

# Numerical Study on Flow Around Modern Ship Hulls with Rudder-Propeller Interactions

Md. Mashud Karim<sup>1</sup> · Nabila Naz<sup>1</sup>

Received: 20 November 2017 / Accepted: 7 September 2018 / Published online: 12 November 2019  
© Harbin Engineering University and Springer-Verlag GmbH Germany, part of Springer Nature 2019

## Abstract

Reducing the fuel consumption of ships presents both economic and environmental gains. Although in the past decades, extensive studies were carried out on the flow around ship hull, it is still difficult to calculate the flow around the hull while considering propeller interaction. In this paper, the viscous flow around modern ship hulls is computed considering propeller action. In this analysis, the numerical investigation of flow around the ship is combined with propeller theory to simulate the hull-propeller interaction. Various longitudinal positions of the rudder are also analyzed to determine the effect of rudder position on propeller efficiency. First, a numerical study was performed around a bare hull using Shipflow computational fluid dynamics (CFD) code to determine free-surface wave elevation and resistance components. A zonal approach was applied to successively incorporate “potential flow solver” in the region outside the boundary layer and wake, “boundary layer solver” in the thin boundary layer region near the ship hull, and “Navier-Stokes solver” in the wake region. Propeller open water characteristics were determined using an open-source MATLAB code OpenProp, which is based on the lifting line theory, for the moderately loaded propeller. The obtained open water test results were specified in the flow module of Shipflow for self-propulsion tests. The velocity field behind the ship was recalculated into an effective wake and given to the propeller code that calculates the propeller load. Once the load was known, it was transferred to the Reynolds-averaged Navier-Stokes (RANS) solver to simulate the propeller action. The interaction between the hull and propeller with different rudder positions was then predicted to improve the propulsive efficiency.

**Keywords** Free-surface wave · Wake · Self-propulsion characteristics · Ship flow · Computational fluid dynamics · Zonal approach · RANS · Rudder-propeller interaction · Ship hulls

## Article Highlights

- To ensure economic and environmental gains, the flow around ship hull must be analyzed considering the rudder-propeller interaction.
- Flow around two different modern ship hulls with the presence of propellers has been numerically studied at different longitudinal positions of the rudder.
- The zonal approach has been implemented to incorporate the combined effect of the flow around ship hull with the rudder and propeller interaction.
- The propeller and hull efficiencies can be improved by increasing the longitudinal position of the rudder from the propeller which leads to reduced interaction effect.

✉ Md. Mashud Karim  
mashudbuet@gmail.com

<sup>1</sup> Department of Naval Architecture and Marine Engineering,  
Bangladesh University of Engineering and Technology,  
Dhaka, Bangladesh

## 1 Introduction

Determining the resistance and propulsive characteristics of ships have always been a great concern at all stages of ship design, both for naval architects and shipbuilders. The main target of shipbuilding in the twenty-first century is to design ships with more fuel efficiency and less pollutant and greenhouse gas emission, which will ultimately reduce transportation cost without harming the environment. Due to a great emphasis on economic and environmental efficiency, designers are forced to optimize the existing solutions and search for new designs.

To design a more fuel-efficient ship, the naval architects or ship designers need to predict the power requirement of ships, which depends on how much resistance the ships have to overcome in a seaway. Thus, to determine such resistance and predict the power requirement, the features of the flow

around the ship hull must be well understood and measured accurately in a way that designers can try many hulls and propulsion arrangements without spending too much time, effort, and resources.

Hence, ship designers need to investigate the hydrodynamic performance of ships with rudder-propeller interactions. Estimating bare hull resistance is the first step toward knowing the performance of the ship in a seaway, and this can be efficiently computed using a large number of numerical methods. The propeller open water characteristics can be successfully determined by various computational methods, e.g., vortex lattice method and boundary element method. However, simulation of self-propulsion test has not yet been fully established because of the difficulty in calculating the effective wake. The presence of rudder affects the wake generated by ship and propeller. Propeller performance can be changed depending on various rudder positions. Based on the present emphasis on increased ship speeds, the flow around ship hull with rudder-propeller interactions has attracted researchers for the improvement of ships performance. There are mainly three ways to predict resistance and propulsive factors, which include empirical methods, physical experiments, and numerical methods. Initially, this prediction was carried out based on a set of empirical methods (Michell 1898), model testing (Takeshi et al. 1987), and wind tunnel (Gietz and Kux 1995) experiments. Among them, model testing is considered as the most reliable and accurate method for ship performance prediction. Among recent experimental investigations, Øyan (2012) and Kayano et al. (2013) determined a ship propulsive performance; they predicted the speed and powering of ships based on a model test using the load-varying self-propulsion method. However, this method is very costly and time-consuming.

At present, computational fluid dynamics (CFD) methods have been developed to a stage where they become interesting, not only from a financial perspective but also from a performance point of view. Due to low memory power of computers, fundamental studies of CFD techniques were initially based on the potential flow theory. Moraes et al. (2004) used the slender body theory of Michell (1898) and CFD-based 3D potential panel method to determine the wave resistance of catamarans. After maturing itself in time, potential flow solver allows the inclusion of free surface into the



Fig. 1 Cartesian coordinate system

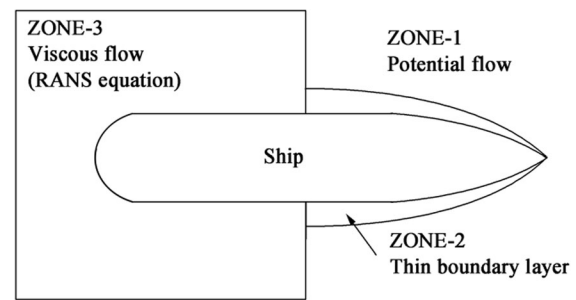


Fig. 2 Zonal approach

problem. Naz and Karim (2017) investigated the hydrodynamic characteristics of high-speed vessels with free-surface and shallow water effects using a potential flow solver. Ghassemi and Ghadimi (2008) used the panel method to predict the hydrodynamic performance of a propeller-rudder system and an azimuthing podded drive system. Their results agreed well with the experiments. With the developments in computational power, the use of Reynolds-averaged Navier-Stokes (RANS) solvers, which allow solving for the viscous flows around ships, have become widespread. Tezdogan et al. (2015) successfully used a full-scale unsteady RANS solver to estimate ship performance in waves. As computer capabilities extend, appendages such as propeller/rudder are also considered in the solutions. During the earlier implementation of RANS solver, Stern and Kim (1994) validated a viscous flow method for predicting a propeller-hull interaction through extensive experimental data. Although recent validation of viscous solver makes the potential solver obsolete, the successful implementation of the viscous solver to analyze complex flow around ship hull with the rudder-propeller interaction requires in-depth knowledge of CFD along with high computational facilities. Therefore, a large number of studies have been carried out to gain insights on the key mechanisms governing the complex interactions among the hull, propeller and rudder.

Different researchers use different numerical approaches and meshing techniques to solve this complex flow feature. Several researchers have used the RANS-BEM method, in which the viscous flow around the hull is solved using a RANS code and the flow around the

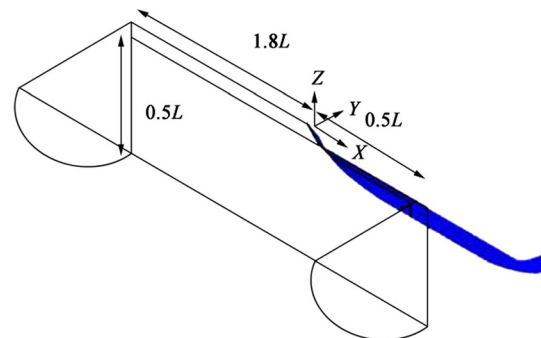


Fig. 3 Computational domain for viscous flow solver

**Table 1** Boundary conditions

Description	$u$	$p$	$k$	$\omega$
No slip wall	$u_i = 0$	$\frac{\partial p}{\partial \xi_b} = 0$	$k = 0$	$\omega = f(u_r)$
Slip wall	$u_i n_i = 0$ $\frac{\partial u_i}{\partial \xi_b} = 0$	$\frac{\partial p}{\partial \xi_b} = 0$	$\frac{\partial k}{\partial \xi_b} = 0$	$\frac{\partial \omega}{\partial \xi_b} = 0$
Inflow	$u_i = \text{const}$	$\frac{\partial p}{\partial \xi_b} = 0$	$k = \text{const}$	$\omega = \text{const}$
Outflow	$\frac{\partial u_i}{\partial \xi_b} = 0$	$p = 0$	$\frac{\partial k}{\partial \xi_b} = 0$	$\frac{\partial \omega}{\partial \xi_b} = 0$

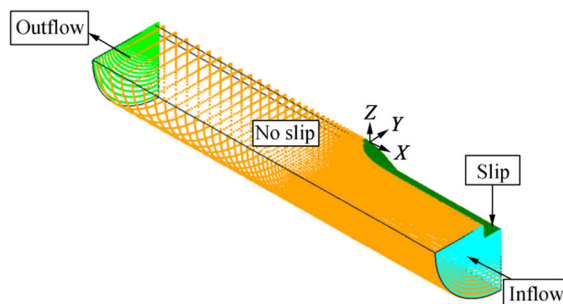
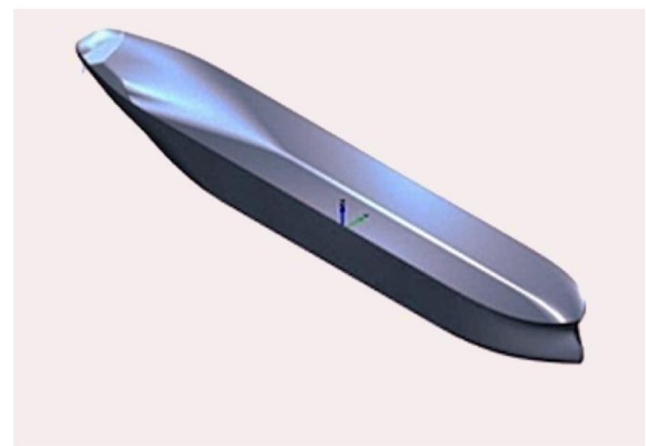
propeller is solved with BEM. The coupling between two codes is done through a two-way coupling: interpolation of the propeller-induced velocities from BEM in RANS and imposing the total wakefield from RANS in the BEM. Phillips et al. (2008) focused on the RANS-BEM for an autonomous underwater vehicle. Karim and Naz (2017) computed self-propulsion characteristics for benchmark ship hulls using RANS-BEM.

Another well-known method is the full RANS method, in which the flows around both ship and propeller are solved in a RANS code. This is accomplished using sliding interfaces: the connection between the rotating grid block around the propeller and the ship-fixed grid around the hull. Zhang (1990) computed the viscous flow around the model ship using a RANS solver for three different grid sets. Then he considered the effect of an operating propeller by applying body force and sliding mesh approaches. Carrica et al. (2010) proposed a method that involves using the speed controller of propeller and dynamic overset grids to find the self-propulsion point to reach the target speed.

Kim et al. (2006), Krasilnikov (2013), and Rijpkema et al. (2013) used a numerical simulation method based on hybrid RANS and potential flow theory to predict the self-propulsion performance of ships. Sakamoto and Kume (2016) and Kawabuchi et al. (2016) used unsteady RANS-based CFD simulation with a sliding grid technique to determine the hull-propeller interaction. Recently, Sezen et al. (2018) investigated the resistance and self-propulsion of the benchmark DARPA Suboff with a E1619 propeller by combining body force and RANS methods. Though these methods guarantee accuracy, the time required to calculate the interaction at a single speed is too long, and it is only possible using a

high-performance supercomputer. Moreover, the effect of changing the rudder position on the propulsive characteristics of ships was not considered in their work.

In this paper, the flows around two modern benchmark ship hulls, namely Kiso Container Ship (KCS) and Japan Bulk Carrier (JBC), are computed with the self-propulsion characteristics of KP505 and DTMB 4119 propellers, respectively (Larsson et al. 2015). Semi-balanced horn-type rudder at different positions was modeled to determine the effect of rudder position on propulsive characteristics. The ship hull geometry was represented by a single block-structured grid of H-O type. Additional grids for the propeller and rudder were fitted with the hull by the overlapping grid generation technique. Verification and validation study along with uncertainty

**Fig. 4** Boundary types for computational domain**(a) KCS****(b) JBC****Fig. 5** Description of the hull

**Table 2** Principal particulars for KCS and JBC hulls

Hull type	Main particulars	Length between perpendiculars (m)	Maximum beam of waterline (m)	Depth (m)	Draft (m)	Block coefficient ( $C_B$ )
KCS	Full	230.0	32.2	19.0	10.8	0.651
	Model	7.279	1.0190	0.6019	0.342	0.651
JBC	Full	280.0	45.0	25.0	16.5	0.859
	Model	7.0	0.561	0.630	0.423	0.859

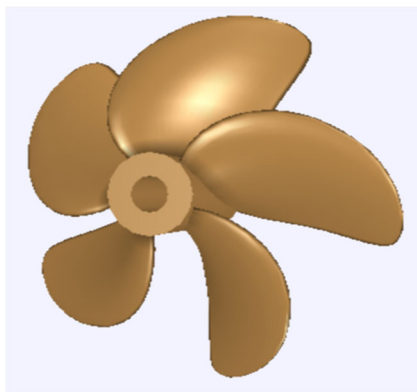
assessment for resistance and open water characteristics were performed. For turbulence modeling,  $k-\omega$  shear-stress transport (SST) model without wall functions (Menter 1994) was used with the RANS solver. Finite volume method was used to discretize the governing equations, which are solved iteratively with alternating direction implicit solver using a computer software Shipflow (Broberg et al. 2007).

The RANS computations included the propeller action by applying the body force method. The method considered the thrust and torque of the propeller as a field of forces, which can be added to the body force terms in the RANS equations. The propeller forces were calculated using the lifting line theory (Flood 2009). A computer program based on this theory was utilized using OpenProp MATLAB code to determine propeller open water characteristics (Epps and Kimball 2013). The open water performance curves of OpenProp were used for self-propulsion simulation with Shipflow results. Moreover, different longitudinal rudder positions were investigated and compared to improve propulsive performance. Finally, numerical simulation results are compared with the available published results.

## 2 Numerical Method and Theory

### 2.1 Coordinate System

The coordinate system ( $x, y, z$ ) is located in the undisturbed free surface at the fore perpendicular (F.P) of the hull so that

**Fig. 6** CAD model of KP 505 propeller

the undisturbed incident flow with a constant speed  $U$  appears to be streaming in the positive  $x$ -direction, with  $y$ -axis extending to the starboard side and  $z$ -axis upward, as shown in Fig. 1.

### 2.2 Zonal Approach

To efficiently compute the flow around a ship, a zonal approach is used, as shown in Fig. 2, in which the flow around a ship is divided into three different zones with different solution methods. The region outside the boundary layer and wake is considered to be incompressible, inviscid, and irrotational. Therefore, in the outer flow (zone 1), the potential flow theory is employed. The inner flow is divided into a thin boundary layer (zone 2) and stern/wake region (zone 3).

### 2.3 Governing Equation

To compute the flow around a ship hull, three types of governing equations are used depending on the hypothesis and considerations assumed in the different regions. For potential flow region, it is assumed that the fluid is incompressible and inviscid and the flow is irrotational. Consequently, the continuity equation becomes the following:

$$\nabla^2 \phi = 0 \quad (1)$$

where  $\nabla$  is the Laplace operator and  $\phi$  is the velocity potential. Here, the potential flow panel method based on Rankine sources is implemented with the hull and nonlinear free-surface boundary conditions. The thin boundary layer near the hull is computed with momentum integral equation:

**Table 3** KP 505 propeller blade main properties

Parameter	Principal dimension
Number of blades	Five
Section profile	NACA66 thickness form + $a = 0.8$ mean line
Propeller diameter	7.9 m (model: 250 mm)
Hub ratio	0.180
Blade area ratio	0.80

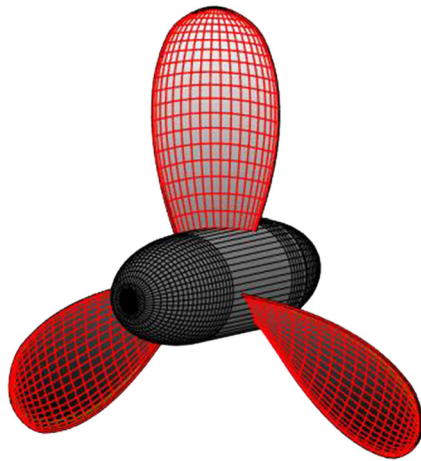


Fig. 7 OpenProp model of DTMB 4119 propeller

$$\frac{d\theta}{dx} + \frac{\theta}{u} \cdot (H + 2) \frac{dU}{dx} = \frac{C_f}{2} \quad (2)$$

where  $\theta$ ,  $H$ ,  $C_f$  denote momentum thickness, shape factor, and friction coefficient, respectively. The viscous flow at the stern region is solved using steady RANS equations coupled with the time-averaged continuity equation:

$$\frac{\partial \bar{u}_i}{\partial x_i} = 0 \quad (3)$$

$$\frac{\partial}{\partial x_j} (\bar{u}_i \bar{u}_j) = -\frac{1}{\rho} \frac{\partial \bar{p}}{\partial x_i} + F_i + \frac{1}{\rho} \frac{\partial}{\partial x_j} (\bar{\sigma}_{ji} + R_{ji}) \quad (4)$$

where  $\bar{u}_{i(j)}$ ,  $\bar{p}$ ,  $\bar{\sigma}_{ji}$ ,  $\rho$ ,  $F_i$  denote the average velocity, pressure, stress, water density, and body force, respectively.

In the left-hand side of the time-averaged Navier-Stokes Eq. (4), the convective term has a new tensor unknown  $R_{ji} = -\rho \overline{u'_i u'_j}$  called Reynolds stresses. In total, six additional unknowns are added since  $R_{ji}$  is a symmetric tensor.

Therefore, to solve this closure problem, more equations are needed. The computational procedure that is used to close the system is called turbulence modeling. In this study, the SST  $k-\omega$  model was used to model the turbulence flow.

Table 4 DTMB 4119 propeller blade main particulars

Parameter	Principal dimension
Number of blades	Three
Section profile	NACA66 thickness form + $a = 0.8$ mean line
Propeller diameter (m)	0.3048
Hub ratio	0.26
Blade area ratio	0.66

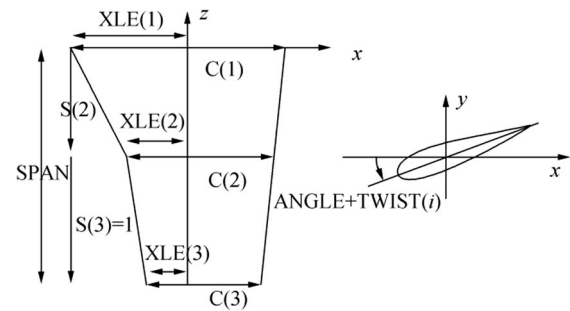


Fig. 8 Geometry definition of semi-balanced horn rudder

**Shear-Stress Transport  $k-\omega$  model** This model was developed by Menter (1994) to effectively blend the robust and accurate formulation of the  $k-\omega$  model in the near-wall region with the free-stream independence of the  $k-\varepsilon$  model in the far field. To achieve this, the  $k-\varepsilon$  model is converted to a  $k-\omega$  formulation. The turbulence kinetic energy,  $k$ , and the specific dissipation rate,  $\omega$ , are obtained from the following transport equations:

$$\frac{\partial}{\partial t} (\rho k) + \frac{\partial}{\partial x_i} (\rho k u_i) = \frac{\partial}{\partial x_j} \left( \Gamma_k \frac{\partial k}{\partial x_j} \right) + G_k - Y_k + S_k \quad (5)$$

$$\frac{\partial}{\partial t} (\rho \omega) + \frac{\partial}{\partial x_i} (\rho \omega u_i) = \frac{\partial}{\partial x_j} \left( \Gamma_\omega \frac{\partial \omega}{\partial x_j} \right) + G_\omega - Y_\omega + S_\omega \quad (6)$$

In these equations,  $G_k$  represents the generation of turbulence kinetic energy due to mean velocity gradients;  $G_\omega$  represents the generation of specific dissipation rate,  $\omega$ ;  $\Gamma_k$  and  $\Gamma_\omega$  represent the effective diffusivity of  $k$  and  $\omega$ , respectively; and  $Y_k$  and  $Y_\omega$  represent the dissipation of  $k$  and  $\omega$  due to turbulence.

## 2.4 Computational Domain for Viscous Flow Solver

Due to the symmetry on the  $x$ - $z$  plane, a quarter of a cylinder is used as the computational domain, with a radius of  $0.5 L$  and a

Table 5 Semi-balanced horn rudder dimension

Particulars	Value
Span (m)	0.36
Angle (°)	0
Origin (x, y, z)	(0, 0, 0.36)
XLE(1)	0.080
XLE(2)	0.060
XLE(3)	0.040
C(1)	0.260
C(2)	0.188
C(3)	0.135
S(1)	0.000
S(2)	0.500
S(3)	1.000



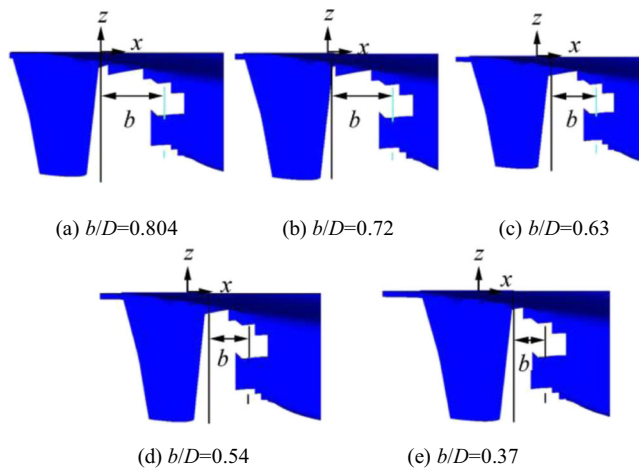


Fig. 9 Different  $b/D$  ratios for the KCS hull

downstream length of  $1.8 L$ , and for the zonal approach, the viscous computation starts from  $0.5 L$  behind the F. P of the ship, as shown in Fig. 3.

## 2.5 Boundary Conditions for Viscous Flow Computation

In the viscous solver, the boundary conditions are implied on the computational domain to solve partial differential equations of RANS solver. The boundary types employed are no slip wall, slip wall, inflow, and outflow (Broberg et al. 2007). Both Dirichlet and Neumann boundary conditions are formulated in terms of pressure  $p$ , velocity  $u_i$ , turbulent kinetic energy  $k$ , and turbulent frequency  $\omega$ . Descriptions of boundary types are given in Table 1 and Fig. 4. In Table 1  $n_i$ ,  $u_i$ ,  $\xi_B$  denote the normal to the surface, the velocity at characteristics time, and the direction of the parameter crossing the boundary, respectively.

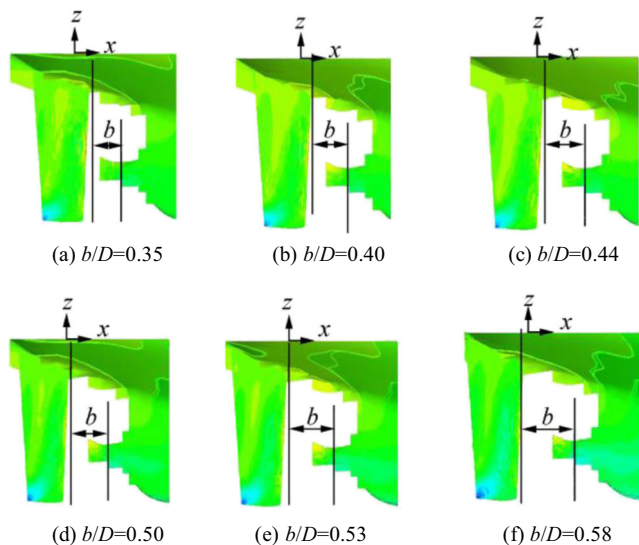


Fig. 10 Different  $b/D$  ratios for the JBC hull

## 2.6 Propeller Theory

Typical propeller characteristics that play an important role in the design are advance coefficient  $J$ , thrust coefficient  $K_t$ , and torque coefficient  $K_q$ . These characteristics are defined as follows:

$$J = \frac{V_A}{nD} \quad (7)$$

$$K_t = \frac{T}{\rho n^2 D^4} \quad (8)$$

$$K_q = \frac{Q}{\rho n^2 D^5} \quad (9)$$

The engine-generated power delivered to the propeller, (10)

$$P_D = 2\pi n Q_n$$

In the above,  $V_A$  is advance velocity,  $T$  is thrust,  $Q_n$  is the generated torque, and  $D$  is the propeller diameter.

$$\text{Effective power, } P_E = R_T V_S \quad (11)$$

$$\text{Open water efficiency, } \eta_o = \frac{J K_t}{2\pi K_q} \quad (12)$$

$$\text{Propulsive efficiency, } \eta_D = \frac{P_E}{P_D} \quad (13)$$

$$\text{Effective wake, } V_w = V - V_A \quad (14)$$

$$\text{Wake fraction, } w = \frac{V_w}{V} \quad (15)$$

## 3 Geometry and Condition

### 3.1 Description of Hull

In this study, two modern benchmark ship hulls, namely KCS and JBC, as shown in Fig. 5, were used for CFD validation (Larsson et al. 2015).

The principal particulars in full and model scales are described in Table 2.

### 3.2 Description of Propeller

#### 3.2.1 KP 505 Propeller

For the KCS hull propeller, open water and self-propulsion characteristics were determined for a KP 505 marine propeller (Larsson et al. 2015), which is shown in Fig. 6.

The main properties of the propeller blades are described in Table 3.

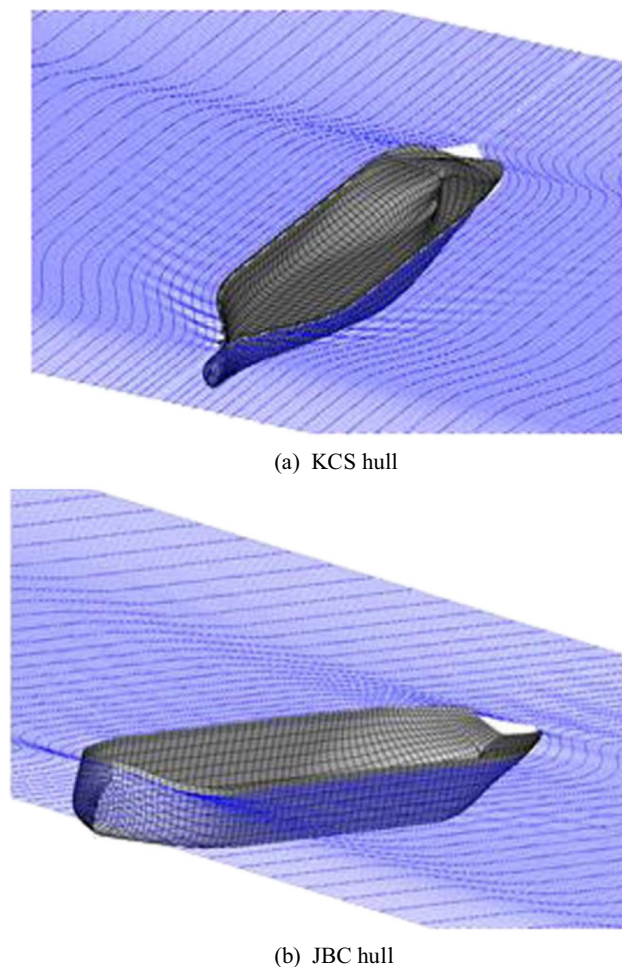


Fig. 11 Discretization of hulls and free surface

### 3.2.2 DTMB 4119 Propeller

For the JBC hull propeller, open water and self-propulsion characteristics were determined using a DTMB 4119 (Belhenniche and Kadda 2016) marine propeller, which is shown in Fig. 7. The main properties of the propeller blades are shown in Table 4.

### 3.3 Description of Rudder

To determine the effect of rudder position on self-propulsion characteristics of the propeller, a semi-balanced horn rudder was used for both ships. The geometry of the rudder is defined in Fig. 8.

A detailed description of the semi-balanced horn rudder dimension is presented in Table 5.

### 3.4 Longitudinal Position of Rudder from Propeller

To determine self-propulsive characteristics at various longitudinal rudder positions, different longitudinal distances of the rudder ( $b$ ) to the propeller diameter ( $D$ ) were taken. The

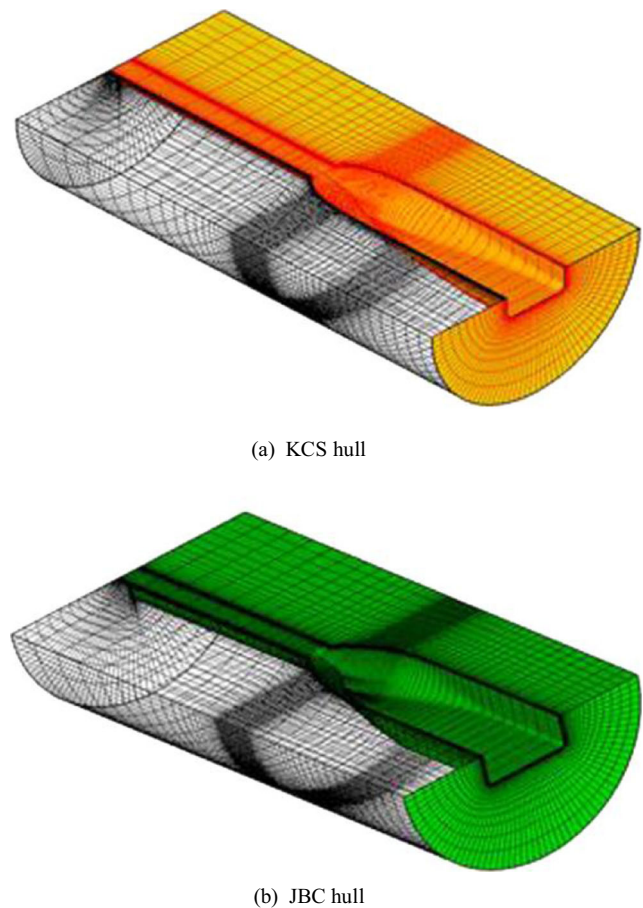


Fig. 12 Single block-structured grid of H-O type around the bare ship hull

different  $b/D$  ratios for KCS and JBC hulls are defined in Figs. 9 and 10, respectively.

To achieve a balance between thrust and drag, the result of self-propulsion test was implemented by adjusting the  $J$  value. The wave drag computed by the potential flow

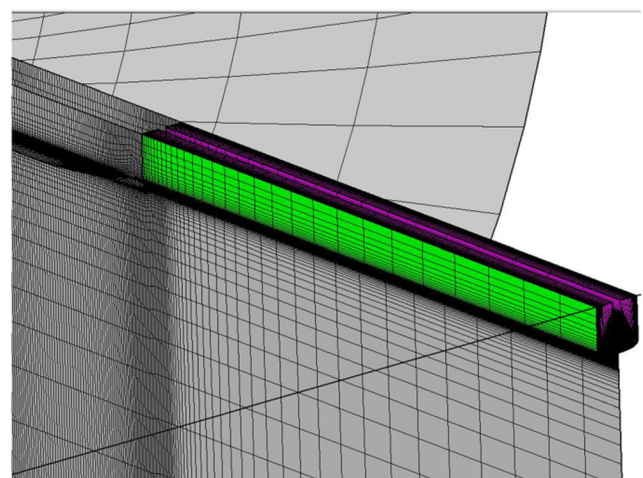
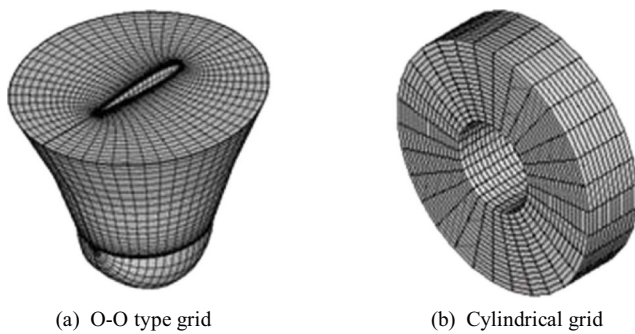


Fig. 13 Additional grid at transom stern of the KCS hull





**Fig. 14** Grid around rudder and propeller

method was included in the total drag. As the zonal approach was used for computing flow around the ship hull with propeller and rudder, the frictional drag was computed by the thin boundary layer for the forebody and was also added to the total drag. The external tow force was then subtracted from the drag. The towing force was computed according to the International Towing Tank Conference (ITTC) 78 procedure. The towing force coefficient,  $CWTO$ , was calculated using Eq. (16) and imported as input data into computation.

$$CWTO = CF_m - (CF_s + dCF_s) \quad (16)$$

$$CF = \frac{0.075}{(\log R_{nL} - 2)^2} \quad (17)$$

where  $CF_s$  and  $CF_m$  are the ITTC57 friction drag coefficients for model and ship, respectively, and  $dCF_s$  is a correction depending on the surface condition of the ship.

## 4 Results and Discussions

In this section, the research results are discussed. First, the results of the potential flow solution are presented. After discretizing the inviscid region with flat quadrilateral panels,

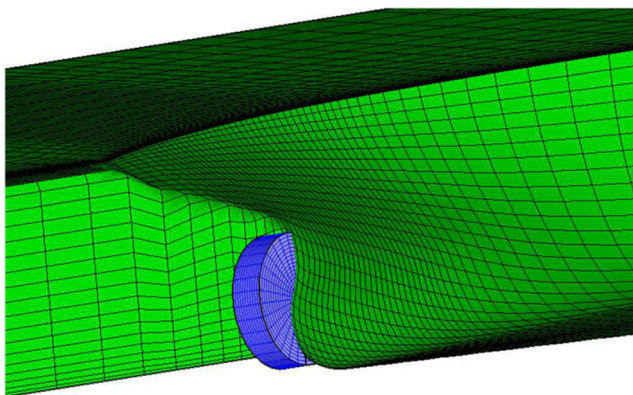


**Fig. 15** Overlapping grid of propeller disc with the ship hull

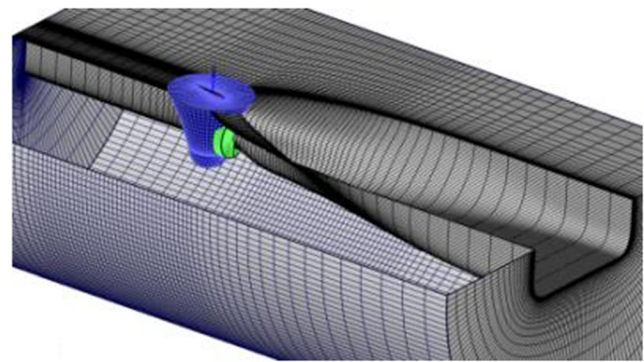


**Fig. 16** The whole grid around rudder-propeller overlapped with the ship hull

the pressure coefficient on hulls, free-surface wave pattern, and wave elevation were obtained as the outcome of the potential flow solution. Wave cuts were obtained at different transverse locations using a viscous flow solver by capturing the free surface with the volume of fluid (VOF) method. The RANS method was used at the stern region where the viscosity effect was significant.

Propeller open water performance curves were obtained through the lifting line program coupled with RANSE solver to determine self-propulsion characteristics at various rudder positions. The zonal and global approaches were compared to outline the efficiency of the present approach.

### 4.1 Panel Mesh Generation for Potential Flow Solver

The nonlinear free-surface potential flow problem was solved by discretizing the hull and the free surface by flat quadrilateral panels with constant source strength, as shown in Fig. 11.

An equation corresponding to the boundary condition was applied to one point on each panel, which gave  $N$  points with  $N$  equations, and  $N$  unknown source strengths. Solving this system of equations, the velocity at every point in the flow was calculated to obtain the potential flow around the hull.

### 4.2 Grid Generation for Viscous Flow Solver

In the viscous flow module, only structured grids were used. The computational domain along with hull geometry was represented by a single block-structured grid of H-O type with 0.45 M cells, as shown in Fig. 12. When the free surface was captured with the viscous flow solver using the VOF method, an additional grid along the transom stern of the KCS hull was

**Table 6** Number of grids for grid convergence study

Coarse	Medium	Fine
0.148 M	0.423 M	1.247 M



**Table 7** V&V study for the KCS bare hull resistance prediction,  $Re = 1.26 \times 10^7$ ,  $Fn = 0.260$ 

Parameters		EFD ( $D$ )	Grid#3 ( $S_3$ )	Grid#2 ( $S_2$ )	Grid#1 ( $S_1$ )	$U_D$ % $S_1$	$U_{SN}$ %
$C_t \times 10^3$	Value	3.711	3.968	3.763	3.738	1.0	0.715
	$E\%D$		-6.925	-1.401	-0.728		
$C_w \times 10^3$	Value		1.6172	1.4962	1.4952		
$C_v \times 10^3$	Value		2.3508	2.2668	2.2428		

created, as shown in Fig. 13. This additional structured grid at the stern can help to capture wet transom stern effect for free surface.

Grid generation around rudder was conducted using a structured grid of O-O type. The propeller was modeled as an actuator disc and gridded with cylindrical grids, which are shown in Fig. 14. Additional grids for the propeller and the rudder were fitted with the hull by Chimera or overlapping grid generation technique, where complex geometries were added to the hull with geometrically simple grid generation technique. The overlapping grid of propeller disc with ship hull is shown in Fig. 15. The whole grid around the rudder-propeller overlapped with the ship hull is shown in Fig. 16.

**Grid Convergence Study** The first step of CFD verification was a grid convergence study. In this research, three sets of systematically refined grids were generated. The multi-block-structured grid was used. The number of numerical grid is listed in Table 6 for all three sets of grids.

Verification of the total resistance was performed according to ITTC recommended procedures for three different grid densities from fine ( $S_1$ ) to coarse ( $S_3$ ), as shown in Tables 7 and 8 for KCS and JBC, respectively. To determine validation errors, the numerical solutions were evaluated against experimental data. Experimental fluid dynamics (EFD) result and data uncertainty were provided for  $C_T$ , and  $U_D$  was obtained as 1% of experimental value ( $D$ ) reported by NMRI (Larsson et al. 2015).

In Figs. 17 and 18, the green long vertical bars represent the data uncertainties ( $U_D$ ), while black short vertical bars denote the numerical uncertainties ( $U_{SN}$ ). From Tables 7 and 8, it is observed that from coarse grid to finer grids, CFD predictions got closer to EFD measurement ( $D$ ).

**Table 8** V&V study for the JBC bare hull resistance prediction,  $Re = 7.46 \times 10^6$ ,  $Fn = 0.142$ 

Parameters		EFD ( $D$ )	Grid#3 ( $S_3$ )	Grid#2 ( $S_2$ )	Grid#1 ( $S_1$ )	$U_D$ % $S_1$	$U_{SN}$ %
$C_t \times 10^3$	Value	4.289	4.175	4.196	4.22	1.0	0.825
	$E\%D$		2.658	2.168	1.61		
$C_w \times 10^3$	Value		0.313	0.3318	0.3318		
$C_v \times 10^3$	Value		3.862	3.864	3.868		

### 4.3 Coefficient of Pressure on the Ship Hull

The hull pressure coefficient was obtained from the potential flow solution by integrating pressure on the hull surface.

Figure 19 shows coefficients of pressure on KCS and JBC hulls at  $Fn = 0.316$  and  $0.142$ , respectively. Both hulls show that the maximum pressure occurred at the bow of the ship where the velocity was minimum.

### 4.4 Free-Surface Wave Pattern

#### 4.4.1 Potential Flow Solver for the KCS Bare Hull

Free-surface wave pattern around KCS at  $Fn = 0.26$  was computed from potential flow solver using a 3D Rankine source panel method and was compared with the measured results from the experiment (Kim et al. 2001), as shown in Fig. 20.

From Fig. 20, it is apparent that both computed wave patterns agreed well with the measured one. However, at the stern region, some discrepancies were observed. At the stern region, the viscosity effect was significant; moreover, the presence of wet transom stern can make the wave pattern from potential flow solver to deviate from the experimental wave pattern.

#### 4.4.2 Viscous Flow Solver for the KCS Bare Hull and Hull with the Rudder and Propeller

When the global approach is applied, viscous/RANS solver is used throughout the whole domain considering rudder-propeller interaction. With the global approach, only the results for very coarse or coarse grids can be obtained. Here, viscous free surface with VOF method was applied with a coarse grid for the bare hull and a very coarse grid for the hull with the rudder-propeller interaction, as shown in Figs. 21 and 22, respectively.

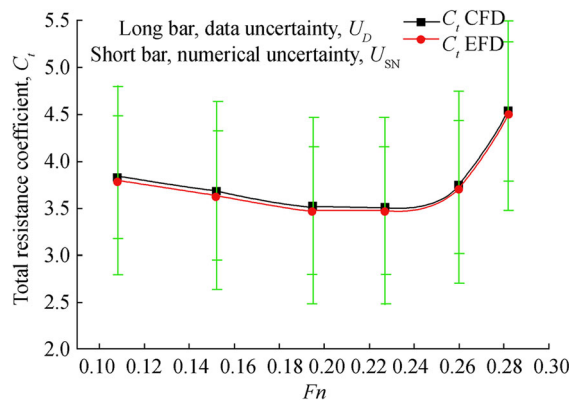


Fig. 17 Verification and validation for resistance coefficients for KCS

It was found that the viscous free surface for both the bare hull and hull with the rudder and propeller showed some changes in a wave pattern. However, the wave pattern did not show any contour at the very far away from the ship's stern, which may be due to very coarse grids of the domain. As the global approach of Shipflow only provides a result for coarse grids due to limitation of computational resources, this approach cannot be used to accurately predict the wave pattern.

#### 4.4.3 Potential Flow Solver for the JBC Bare Hull

The computed wave pattern at  $Fn = 0.142$  around the JBC hull starboard side showed good agreement with the experimental wave pattern obtained by Sakamoto and Kume (2016), as shown in Fig. 23.

#### 4.4.4 Viscous Flow Solver for the JBC Bare Hull and Hull with the Rudder and Propeller

Viscous free surface with VOF method was applied with a coarse grid for bare hull and a very coarse grid for the hull with the rudder-propeller interaction, as shown

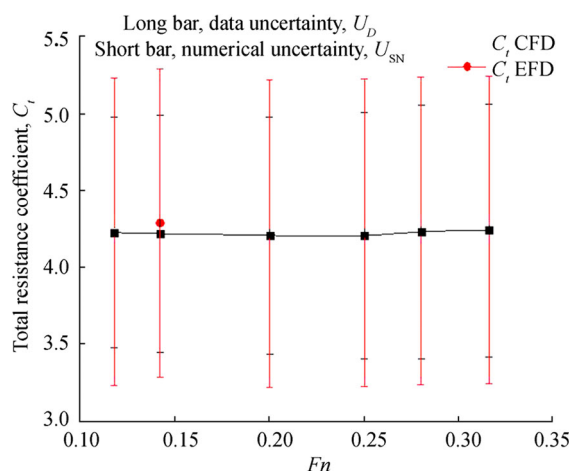
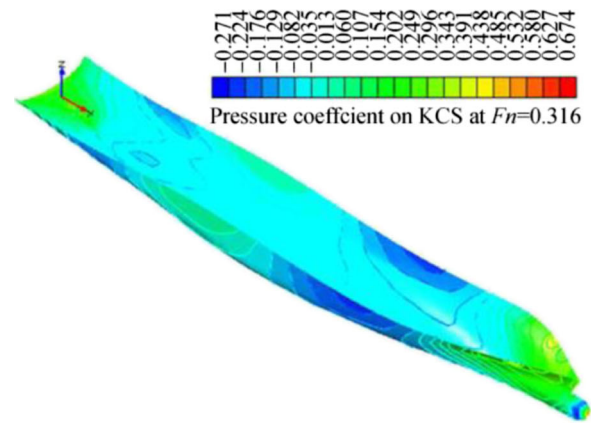
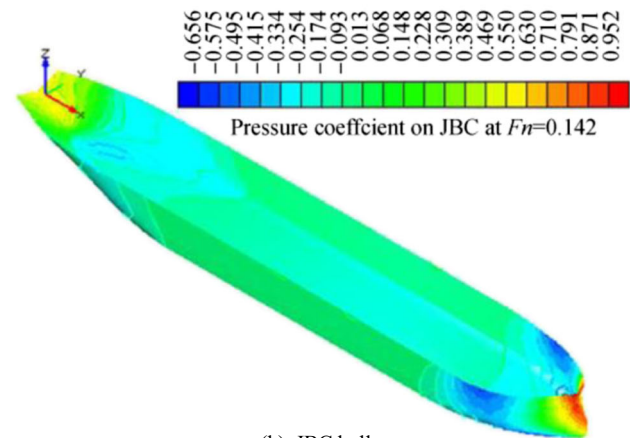


Fig. 18 Verification and validation of resistance coefficients for JBC



(a) KC Shull



(b) JBC hull

Fig. 19 Pressure coefficient on the ship hull

in Figs. 24 and 25, respectively. From those figures, it is found that viscous free surface for both the bare hull and hull with the rudder and propeller showed some changes in the wave pattern. The maximum value of the wave height/length ratio was obtained at the bow and stern of the ship.

## 4.5 Free-Surface Wave Elevations

### 4.5.1 Wave Elevation for KCS

The computed free-surface wave elevations from the potential flow solver around the KCS hull at  $Fn = 0.26$  is shown in Fig. 26. Here, the computed result is also compared with experimental results (Kim et al. 2001).

The computed wave elevation along the ship hull showed good agreement with experimental results (Fig. 26). As the computed results are obtained from the potential flow solution, some discrepancies between the computed and experimental wave heights were found at the wake region of the KCS hull.

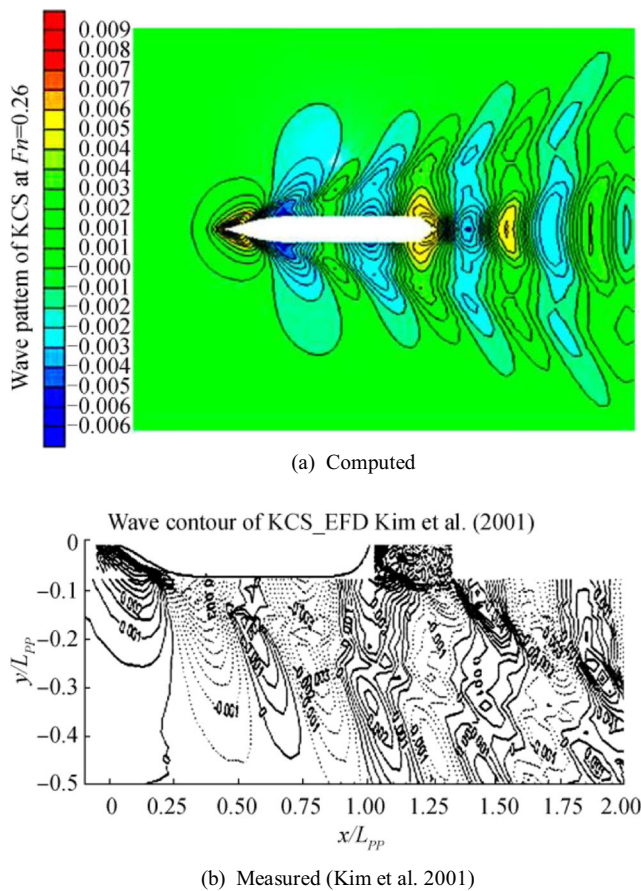


Fig. 20 Wave pattern around the KCS hull at  $Fn = 0.26$

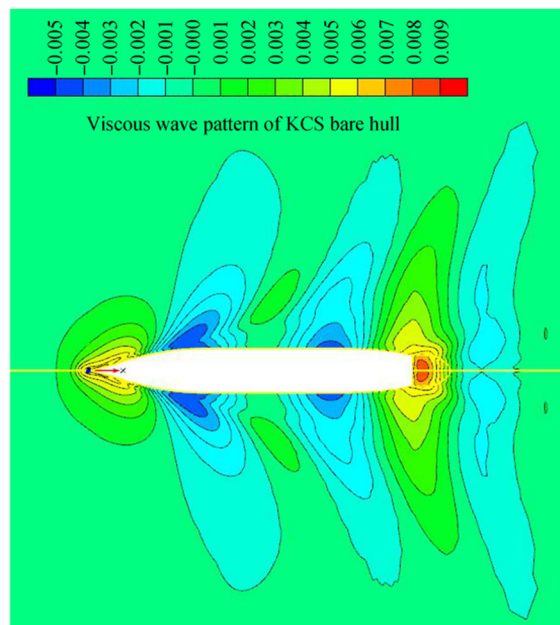


Fig. 21 Viscous wave pattern around the KCS hull at  $Fn = 0.26$

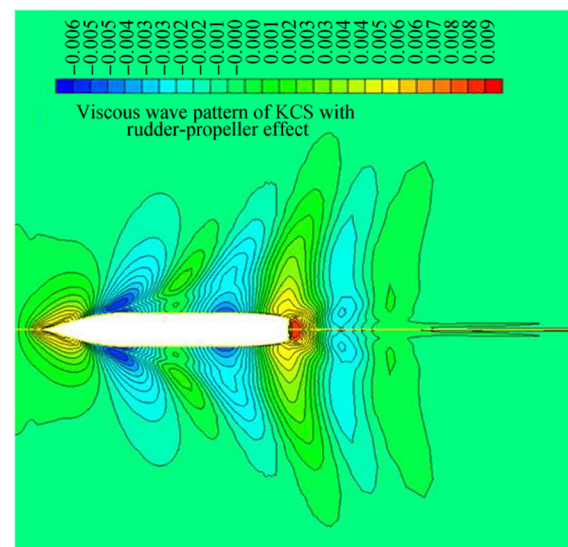


Fig. 22 Viscous wave pattern around the KCS hull with propeller-rudder effect at  $Fn = 0.26$

#### 4.5.2 Wave Elevation for JBC

The computed free-surface wave elevations around the JBC hull at  $Fn = 0.142$  from both the potential flow solver and the experimental results are shown in Fig. 27. It can be observed that the computed wave elevation along the JBC hull agreed well with experimental results obtained by Sakamoto and Kume (2016).

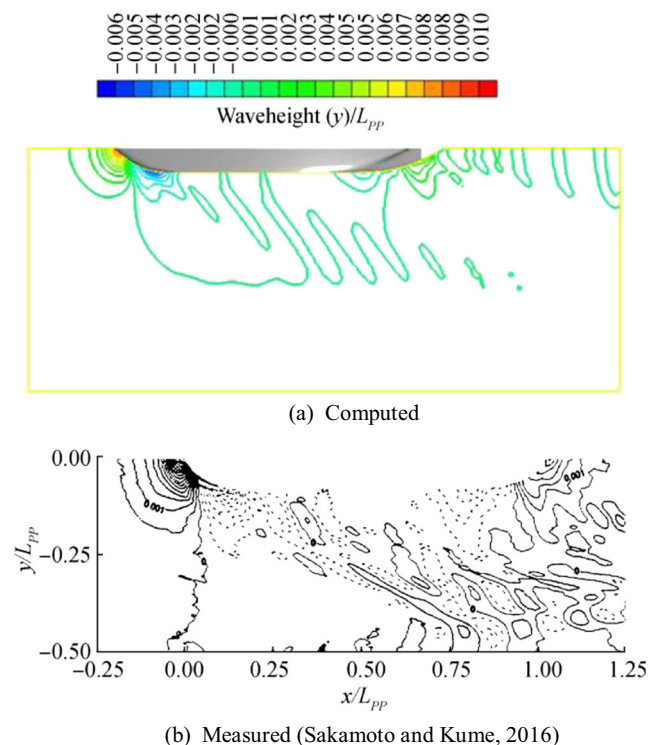


Fig. 23 Wave pattern around the JBC hull at  $Fn = 0.142$

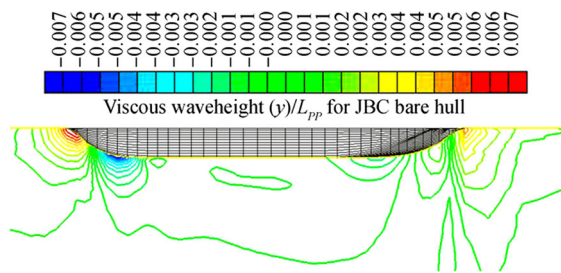


Fig. 24 Viscous wave pattern around the JBC hull  $Fn = 0.142$

#### 4.6 Wave Cuts

Wave cuts were obtained as the intersection of the wave pattern with different planes. Transverse wave cuts with planes separated from the center plane to the portside distances of  $y = -0.1$ ,  $-0.2$ , and  $-0.3$  are shown in Fig. 28 and Fig. 29 for KCS and JBC hulls, respectively.

As the wave cuts moved further away from the ship hull, the magnitude of wave height decreased (Figs. 28 and 29). The maximum wave height/length ( $z/L_{pp}$ ) occurred at transverse plane  $y = -0.1$ , which was the closest transverse cutting plane at the port side, whereas the minimum wave height/length ( $z/L_{pp}$ ) occurred at transverse plane  $y = -0.3$ , which was the furthest transverse cutting plane at the port side.

The comparison results of different wave cuts between the bare hull and hull with the rudder-propeller effect are shown in Figs. 30, 31, and 32 for KCS and Figs. 33, 34, and 35 for JBC.

For the KCS, the value of the wave height remained the same for the bare hull and hull with the rudder-propeller condition until the location of the propeller plane (Figs. 30, 31, and 32). At the propeller plane, which was at  $x = 0.9747$ , the wave height suddenly increased. The maximum increase in wave height occurred when the wave cut was very close to the hull, i.e.,  $y = -0.1$ , as shown in Figs. 30 and 33. At the propeller plane, flow suddenly accelerated, which may lead to an increase of wave height at this location due to a hull-propeller-rudder interaction.

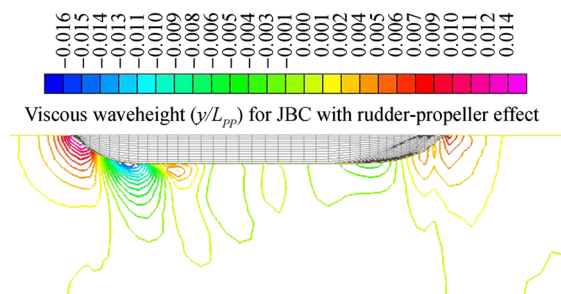


Fig. 25 Viscous wave pattern around the JBC hull with the propeller-rudder effect at  $Fn = 0.142$

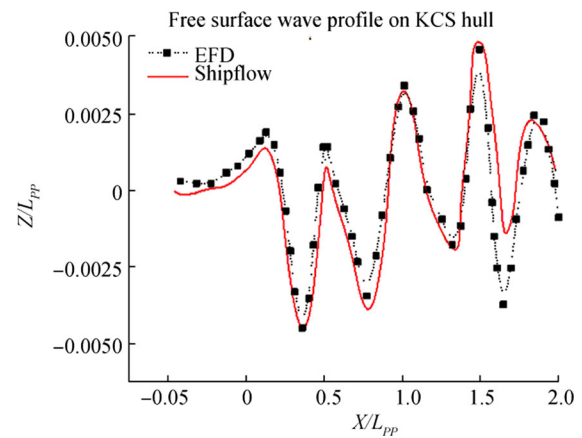


Fig. 26 Free-surface wave elevations around the KCS hull from potential flow solution

#### 4.7 Propeller Open Water Characteristics

Propeller open water characteristics were determined for various advance ratios utilizing an open-source MATLAB code OpenProp (Flood 2009). Forces and moments were calculated in the propeller grid with the lifting line program of OpenProp are applied to the RANS as body forces.

##### 4.7.1 KP 505 Propeller Open Water Results

The propeller performance results for the KP 505 propeller is shown with the solid lines in Fig. 36. The dashed lines represent the experimentally derived performance values as reported by the National Maritime Research Institute, T0215.

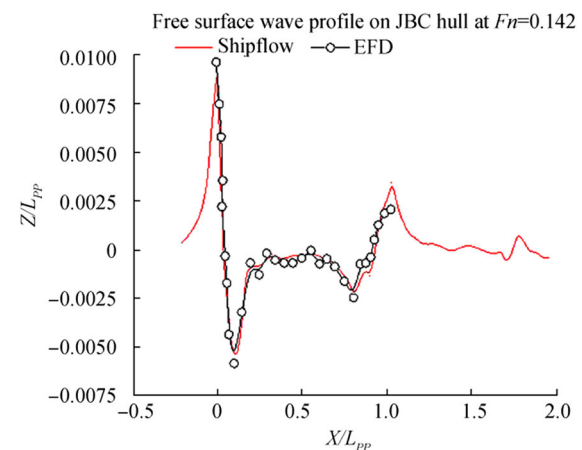
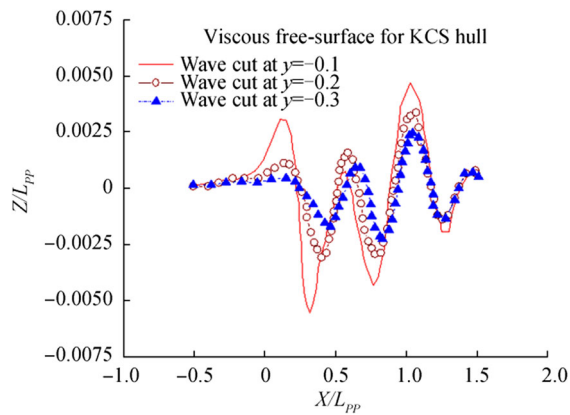


Fig. 27 Free-surface wave elevations around the JBC hull from potential flow solution





**Fig. 28** Transverse wave cuts for the KCS hull at  $Fn = 0.26$

#### 4.7.2 KP 505 Propeller Open Water Uncertainty at $Fn = 0.26$

Uncertainty assessment for KP 505 propeller was conducted by comparing the CFD results with the EFD results provided by Tokyo CFD Workshop (Larsson et al. 2015), as shown in Table 9.

#### 4.7.3 DTMB 4119 Propeller Open Water Results

The propeller performance results for the DTMB 4119 propeller is shown with the solid lines in Fig. 37, while the dashed lines represent the experimentally derived performance values as reported by Koyama (1972).

From Figs. 36 and 37, it is clear that the most significant differences occurred in the torque coefficient and efficiency values at low and high values of the advance ratio. One possible reason for the deviations at low  $J$  values is that the Lerbs lifting line method is only valid for moderately loaded propellers. The load increased with decreasing advance ratio; therefore, error is expected in this region.

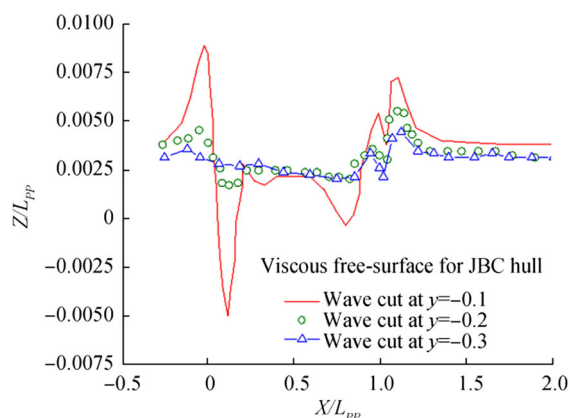


**Fig. 29** Transverse wave cuts for the JBC hull at  $Fn = 0.142$

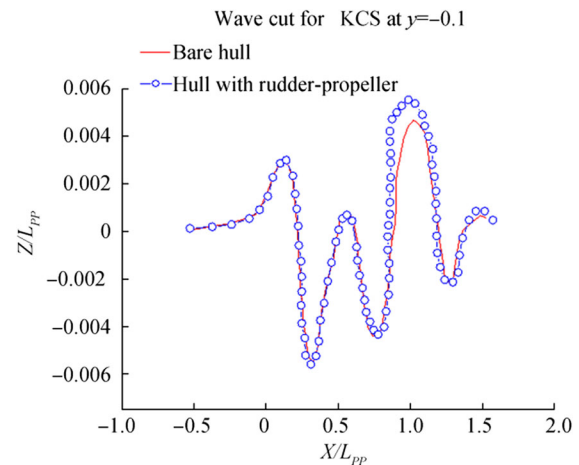


**Fig. 30** Transverse wave cuts for the KCS hull at  $y = -0.1$

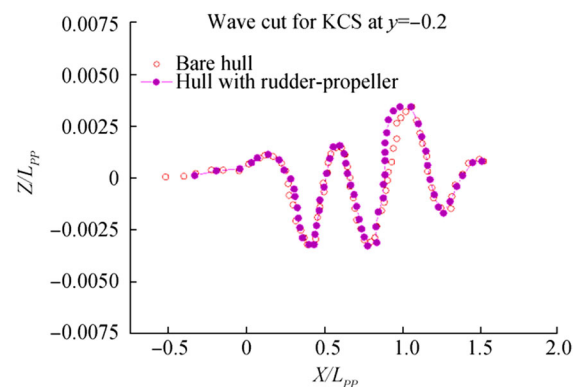
#### 4.7.4 DTMB Propeller Open Water Uncertainty at $Fn = 0.142$

Uncertainty assessment for DTMB 4119 propeller was conducted by comparing the CFD results with the EFD results presented at Tokyo CFD Workshop (Larsson et al. 2015), as shown in Table 10.

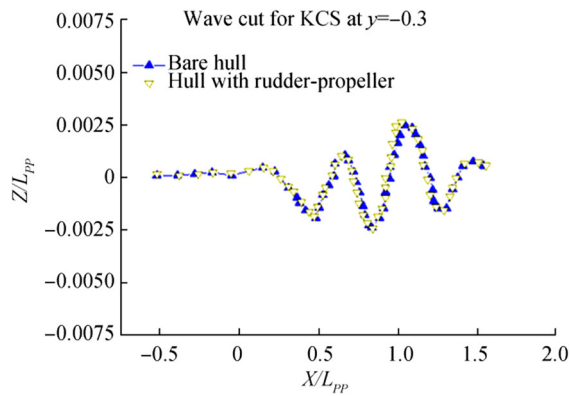
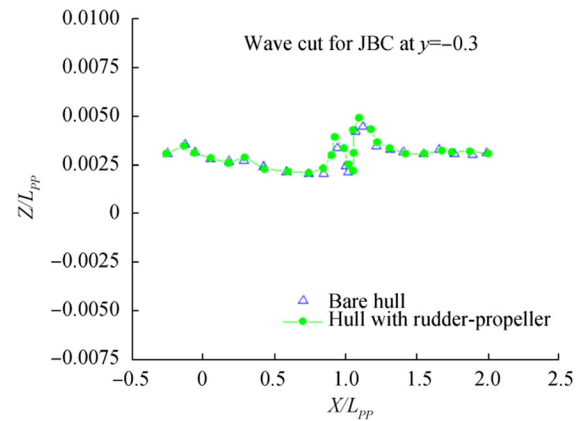
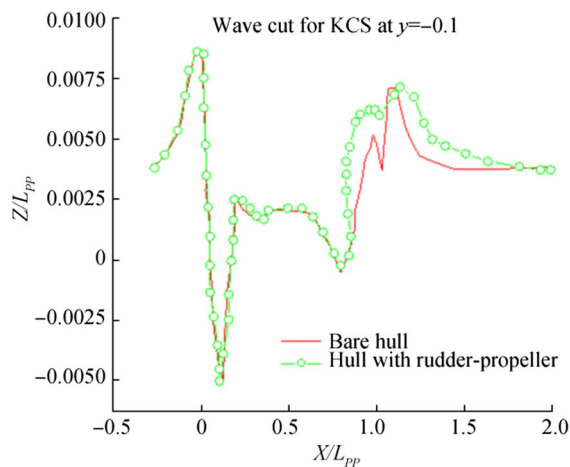
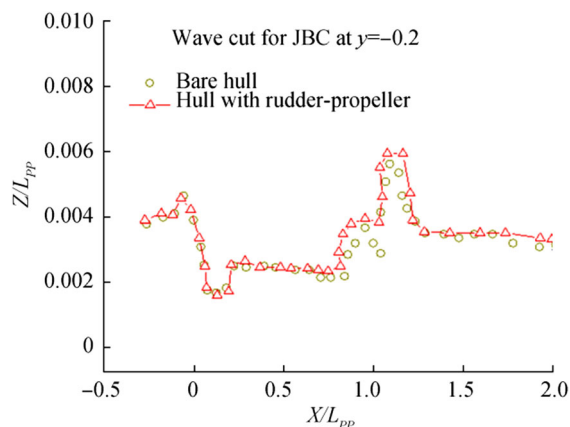
### 4.8 Self-Propulsion Results at Various Rudder Positions

The computed self-propulsion characteristics for KCS and JBC hulls are summarized in Tables 11 and 12.

For both hulls, as the rudder was further away from the propeller, maximum thrust, minimum torque, and minimum resistance were approached. Therefore, with respect to thrust, torque, and resistance, rudder positions ( $b/D$ ) of 0.72 and 0.58 can be considered as optimum for KCS and JBC, respectively. The computed variations of total resistance coefficient  $C_r$ , with different rudder positions, are shown in Figs. 38 and 39 for KCS and JBC, respectively.



**Fig. 31** Transverse wave cuts for the KCS hull at  $y = -0.2$

Fig. 32 Transverse wave cuts for the KCS hull at  $y = -0.3$ Fig. 35 Transverse wave cuts for the JBC hull at  $y = -0.3$ Fig. 33 Transverse wave cuts for the JBC hull at  $y = -0.1$ Fig. 34 Transverse wave cuts for the JBC hull at  $y = -0.2$ 

#### 4.9 Comparison of Computed Axial Velocity Contour with Experimental Results

The numerical solution revealed a rather complex flow field in the stern region where the velocity distribution and propeller loading reflect changes in the flow field. To determine the complex flow field at a stern with the rudder and propeller, axial velocity contours were determined for both hulls.

Axial velocity contour around the KCS and JBC hulls at a stern position of  $x = 0.95$  with rudder is shown in Fig. 40. For both hulls, the computed results from Shipflow CFD showed good agreement with the experimental results obtained by Larsson et al. (2015).

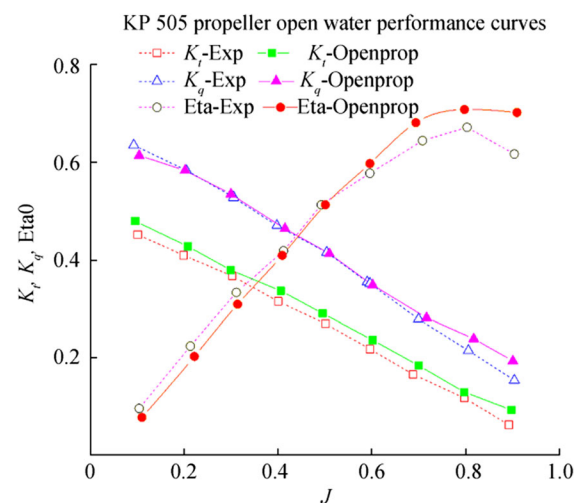


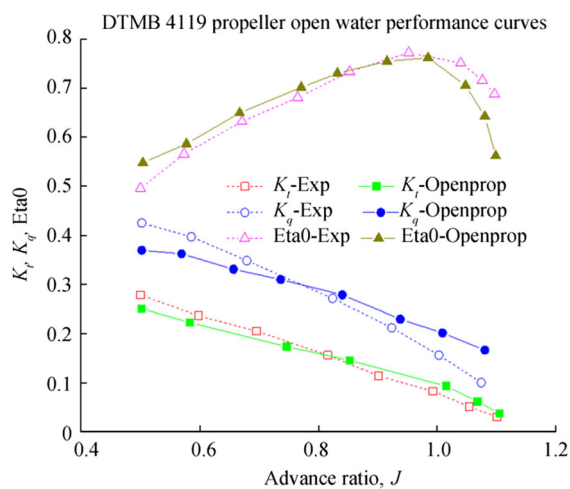
Fig. 36 Open water characteristics of KP 505 propeller

**Table 9** Uncertainty assessment for KP 505 propeller

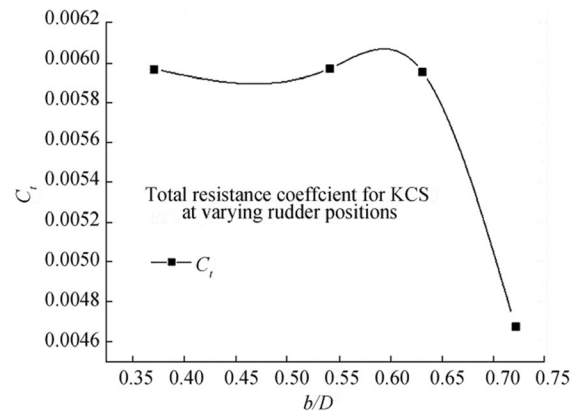
Parameters		CFD	EFD ( $D$ )	$U_D\%$
$K_t$	Value	0.173	0.170	1.0
	$E\%D$		-1.76	
$K_q$	Value	0.0292	0.0288	
	$E\%D$		-1.38	

**Table 10** Uncertainty assessment for DTMB 4119 propeller

Parameters		CFD	EFD ( $D$ )	$U_D\%$
$K_t$	Value	0.214	0.217	1.0
	$E\%D$		1.38	
$K_q$	Value	0.0275	0.0279	
	$E\%D$		1.43	

**Fig. 37** Open water characteristics of DTMB 4119 propeller**Table 11** Self-propulsion characteristics for the KCS hull

$b/D$	$J$	$C_t$	$T$ (kN)	$Q$ (kN·m)
0.37	0.87044	0.00597	4147.98	1167.76
0.54	0.87250	0.00597	4154.3	1168.09
0.63	0.87271	0.00596	4159.7	1163.58
0.72	0.87282	0.00468	4395.65	640.175

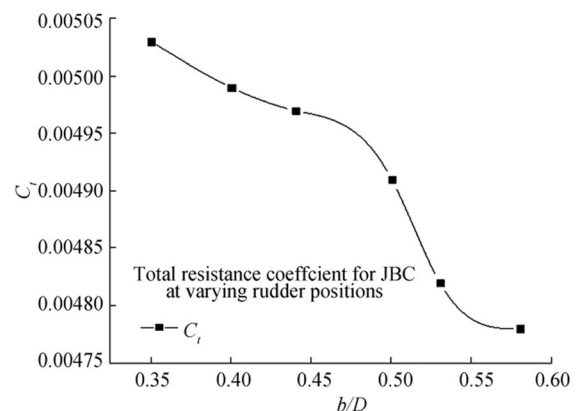
**Fig. 38** Total resistance coefficient for KCS at various rudder positions

#### 4.10 Efficiency of Zonal Approach Over Global Approach

The zonal approach, which was first used to compute the bare ship hull resistance, was compared with the global approach. The former was found to complete the whole analysis in much less time than the latter for very coarse and coarse mesh size. Furthermore, for medium and fine mesh sizes, the zonal approach provided results for both hulls, whereas the global approach is incapable of dealing with similar mesh size, as shown in Table 13. Consequently, it also failed to compute self-propulsion characteristics.

## 5 Conclusions

In this research work, commercial CFD software Shipflow was used to predict the flow around two modern benchmark ship hulls with and without rudder-propeller interaction. Based on the predicted results and discussions, the following conclusions can be drawn as follows:

**Fig. 39** Total resistance coefficient for JBC at various rudder positions

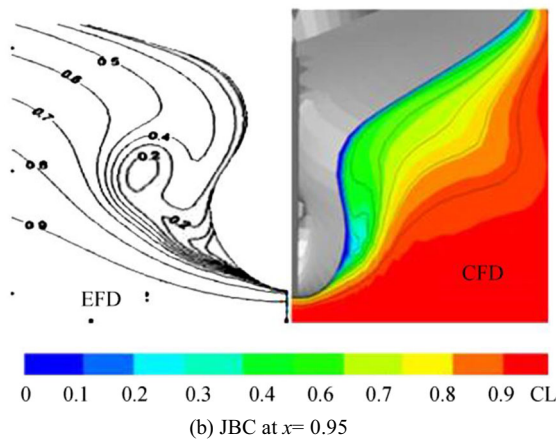
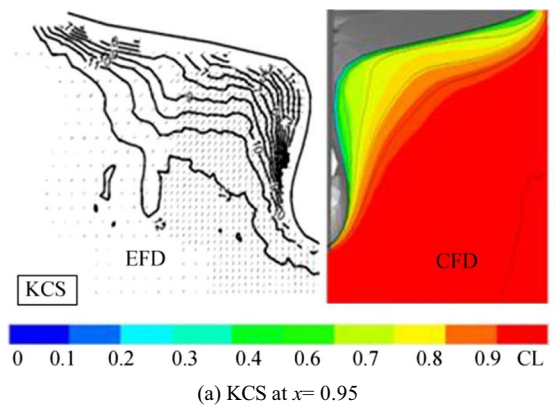


**Fig. 40** Comparison of computed axial velocity contour with EFD at  $x = 0.95$

- 1) The numerical simulation of the flow around bare hull showed significant variation from the hull with rudder and propeller, especially at the stern region. Therefore, to accurately predict flow around ship, the effect of propeller and rudder must not be ignored.
- 2) The computed viscous free-surface wave cuts exhibited more increase in wave height at propeller location for the hull with the rudder and propeller compared to the bare hull, especially when the cutting plane was closer to the hull.
- 3) Axial velocity contours at different upstream and downstream transverse planes of the propeller showed that the

**Table 12** Self-propulsion characteristics for the JBC hull

$b/D$	$J$	$C_t$	$T$ (kN)	$Q$ (kN·m)
0.35	0.86567	0.00503	1449.33	587.309
0.4	0.86613	0.00499	1500.13	585.309
0.44	0.86696	0.00497	1506.78	576.234
0.5	0.86873	0.00491	1512.22	564.832
0.53	0.86909	0.00482	1516.28	559.448
0.58	0.86943	0.00478	1533.29	558.288

**Table 13** Comparison between zonal and global approaches

Mesh size (million, M)	KCS		JBC	
	Zonal time (min)	Global time (min)	Zonal time (min)	Global time (min)
Very coarse (0.213 M)	18	145	18	157
Coarse (0.446 M)	30	230	33	243
Medium (0.744 M)	53	—	57	—
Fine (1.218 M)	77	—	83	—

contour of velocity changed with the change in distance of the cutting plane from the propeller.

- 4) The effect of rudder positions on propulsive characteristics was significant. As the rudder moved far away from the propeller, the interaction effect became less, consequently increasing the propeller efficiency.
- 5) The RANS solver coupled with the lifting line method suitably predicted axial velocity contour to numerically simulate flow around ship considering the hull-propeller-rudder interaction.

**Funding** Authors acknowledge the Committee for Advanced Studies and Research (CASR), Bangladesh University of Engineering and Technology for granting research fund and sub-project CP No. 2084 of Department of Naval Architecture and Marine Engineering under Higher Education Quality Enhancement Project (HEQEP), UGC, Ministry of Education, Govt. of Bangladesh for providing necessary research facilities during the current research work.

## References

- Belhenniche S, Kadda B (2016) Numerical analysis of the turbulent flow around DTMB 4119 marine propeller. *Int J Mar Environ Sci* 10(2): 347–351
- Broberg L, Regnström B, Östberg M (2007) SHIPFLOW theoretical manual. FLOWTECH International AB, Gothenburg
- Carrica PM, Castro AM, Stern F (2010) Self-propulsion computations using a speed controller and a discretized propeller with dynamic overset grids. *J Mar Sci Technol* 15:316–330. <https://doi.org/10.1007/s00773-010-0098-6>
- Epps BP, Kimball RW (2013) OpenProp v3: open-source software for the design and analysis of marine propellers and horizontal-axis turbines. <http://engineering.dartmouth.edu/epps/openprop> (Accessed 22 May 2018)
- Flood KM (2009) Propeller performance analysis using lifting line theory. M.Sc. thesis, Department of Mechanical Engineering, Massachusetts Institute of Technology, Cambridge. 1–60
- Ghassemi H, Ghadimi P (2008) Computational hydrodynamic analysis of the propeller-rudder and the AZIPOD systems. *Ocean Eng* 35:117–130. <https://doi.org/10.1016/j.oceaneng.2007.07.008>



- Gietz U, Kux J (1995) Flow investigations on the Hamburg test case model in the wind tunnel. Institute of Shipbuilding, University of Hamburg, Germany, Report No. 550, 1-52.
- Karim MM, Naz N (2017) Computation of flow field around ship hull including self propulsion characteristics at varying rudder positions. *Procedia Eng*, 10th International Conference on Marine Technology, MARTEC 2016 194:96–103. <https://doi.org/10.1016/j.proeng.2017.08.122>
- Kawabuchi, M, Kubota, M, Ishikawa, S (2016) Development of technology to estimate the flow field around ship hull considering wave making and propeller rotating effects. *Mitsubishi Heavy Industries Technical Review*, 53(2), 53–57.
- Kayano J, Yabuki N, Sasaki N, Hiwatashi R (2013) A study on the propulsion performance in the actual sea by means of full-scale experiments. *Trans Nav Int J Mar Navig Saf Sea Transp* 7:521–526
- Kim WJ, Van SH, Kim DH (2001) Measurement of flows around modern commercial ship models. *Exp Fluids* 31:567–578. <https://doi.org/10.1007/s003480100332>
- Kim J, Kim KS, Kim GD, Park IR, Van SH (2006) Hybrid RANS and potential based numerical simulation for self-propulsion performances of the practical container ship. *J Ship Ocean Technol* 10: 1–11
- Koyama K (1972) A numerical analysis for the lifting surface theory of a marine propeller. *J Soc Nav Architects Jpn* 1972(132):91–98. [https://doi.org/10.2534/jjasnaoe1968.1972.132\\_91](https://doi.org/10.2534/jjasnaoe1968.1972.132_91)
- Krasilnikov VI (2013) Self-propulsion RANS computations with a single-screw container ship. *Third International Symposium on Marine Propulsors*, Launceston, Tasmania, 430–438.
- Larsson L, Stern F, Visonneau M, Hirata N, Hino T, Kim J (2015) *Proceedings of a Workshop on CFD in Ship Hydrodynamics*. NMRI, Tokyo.
- Menter FR (1994) Two-equation eddy-viscosity turbulence models for engineering applications. *AIAA J* 32:1598–1605. <https://doi.org/10.2514/3.12149>
- Michell JH (1898) XI. The wave-resistance of a ship. *Philos Mag* 45:106–123. <https://doi.org/10.1080/14786449808621111>
- Moraes HB, Vasconcellos JM, Latorre RG (2004) Wave resistance for high-speed catamarans. *Ocean Eng* 31:2253–2282. <https://doi.org/10.1016/j.oceaneng.2004.03.012>
- Naz N, Karim MM (2017) Investigation of hydrodynamic characteristics of high speed multihull vessels including shallow water effect. *Procedia Eng* 194:51–58. <https://doi.org/10.1016/j.proeng.2017.08.116>
- Øyan E (2012) *Speed and powering prediction for ships based on model testing*. M.Sc. Thesis, Dept. of Marine Technology, Norwegian University of Science and Technology
- Phillips AB, Turnock SR, Furlong M (2008) Comparisons of CFD simulations and in-service data for the self propelled performance of an autonomous underwater vehicle. *27th Symposium on Naval Hydrodynamics*. 2:951-965, Seoul.
- Rijpkema D, Starke B, Bosschers J (2013) Numerical simulation of propeller-hull interaction and determination of the effective wake field using a hybrid RANS-BEM approach. *Third International Symposium on Marine Propulsors, SMP2013*, Launceston, 421–429
- Sakamoto N, Kume K (2016) Numerical towing tank procedure for JBC in self-propulsion with rotating propeller and energy saving duct. *2016 JASNAOE Spring Annual Meeting*, Fukuoka.
- Sezen S, Dogrul A, Delen C, Bal S (2018) Investigation of self-propulsion of DARPA suboff by RANS method. *Ocean Eng* 150:258–271. <https://doi.org/10.1016/j.oceaneng.2017.12.051>
- Stern F, Kim HT (1994) Computation of viscous flow around propeller-body configurations: series 60  $C_B = 0.6$  Ship Model. *J Ship Res* 38(2):137–157
- Takeshi H, Hino T, Hinatsu M, Tsukada Y, Fujisawa J (1987) ITTC cooperative experiments on series 60 model at ship research institute—flow measurements and resistance tests, vol Supp. 9. *Ship Research Institute*, Japan, 1-481–48
- Tezdogan T, Demirel YK, Kellett P, Khorasanchi M, Incecik A, Turan O (2015) Full-scale unsteady RANS CFD simulations of ship behaviour and performance in head seas due to slow steaming. *Ocean Eng* 97:186-206. doi: 10.1016/j.oceaneng.2015.01.011
- Zhang, D (1990) *Numerical Computation of Ship Stern/Propeller Flow*. PhD thesis, Department of Shipping and Marine Technology, Chalmers University of Technology, Gothenburg.